

Single-Atoms on Crystalline Carbon Nitrides for Selective C–H Photooxidation: A Bridge to Achieve Homogeneous Pathways in Heterogeneous Materials

Marcos A. R. da Silva, Nadezda V. Tarakina, José B. G. Filho, Carla S. Cunha, Guilherme F. S. R. Rocha, Gabriel A. A. Diab, Rômulo Augusto Ando, Oleksandr Savateev, Iker Agirrezabal-Telleria, Ingrid F. Silva, Sara Stolfi, Paolo Ghigna, Maurizio Fagnoni, Davide Ravelli,* Piero Torelli, Luca Braglia, and Ivo F. Teixeira*

Single-atom catalysis is a field of paramount importance in contemporary science due to its exceptional ability to combine the domains of homogeneous and heterogeneous catalysis. Iron and manganese metalloenzymes are known to be effective in C–H oxidation reactions in nature, inspiring scientists to mimic their active sites in artificial catalytic systems. Herein, a simple and versatile cation exchange method is successfully employed to stabilize low-cost iron and manganese single-atoms in poly(heptazine imides) (PHI). The resulting materials are employed as photocatalysts for toluene oxidation, demonstrating remarkable selectivity toward benzaldehyde. The protocol is then extended to the selective oxidation of different substrates, including (substituted) alkylaromatics, benzyl alcohols, and sulfides. Detailed mechanistic investigations revealed that iron- and manganese-containing photocatalysts work through a similar mechanism via the formation of high-valent M=O species. Operando X-ray absorption spectroscopy (XAS) is employed to confirm the formation of high-valent iron- and manganese-oxo species, typically found in metalloenzymes involved in highly selective C–H oxidations.

1. Introduction

Single-atom catalysts (SACs) have garnered significant attention from the scientific community due to their impressive features. These include the exceptional activity and selectivity resulting from their unique electronic structures and active sites' chemical environment.^[1] Additionally, SACs exhibit significant saving in the usage of catalytic metals due to their maximized atom-utilization efficiency.^[1c] Finally, SACs are closely related to homogeneous complexes in that they both involve isolated metal sites within well-defined environments created by organic ligands.^[1c,2] Therefore, analogies with homogeneous catalysts and enzymes can be a starting point for comprehending structure–activity relationships at the atomic-scale in SACs. Also, this

M. A. R. da Silva, C. S. Cunha, G. F. S. R. Rocha, G. A. A. Diab, I. F. Teixeira
Department of Chemistry
Federal University of São Carlos
São Carlos, São Paulo 13565-905, Brazil
E-mail: ivo@ufscar.br

N. V. Tarakina, O. Savateev, I. F. Silva
Department of Colloid Chemistry
Max Planck Institute of Colloids and Interfaces
Am Mühlenberg 1, D-14476 Potsdam, Germany

J. B. G. Filho
Department of Chemistry
ICEx
Federal University of Minas Gerais
Belo Horizonte, MG 31270-901, Brazil

R. A. Ando
Department of Fundamental Chemistry
Institute of Chemistry
University of São Paulo
Av. Prof. Lineu Prestes, 748, São Paulo 05508–000, Brazil

I. Agirrezabal-Telleria
Department of Chemical and Environmental Engineering of the Bilbao
Engineering School
University of Basque Country (UPV/EHU)
Plaza Torres Quevedo 1, Bilbao 48013, Spain

S. Stolfi, P. Ghigna, M. Fagnoni, D. Ravelli
Department of Chemistry
University of Pavia
viale Taramelli 12, Pavia 27100, Italy
E-mail: davide.ravelli@unipv.it

P. Torelli, L. Braglia
TASC Laboratory
CNR–IOM, Istituto Officina dei Materiali
Trieste 34149, Italy

 The ORCID identification number(s) for the author(s) of this article can be found under <https://doi.org/10.1002/adma.202304152>

© 2023 The Authors. Advanced Materials published by Wiley-VCH GmbH. This is an open access article under the terms of the Creative Commons Attribution License, which permits use, distribution and reproduction in any medium, provided the original work is properly cited.

DOI: 10.1002/adma.202304152

resemblance enables the operation of homogeneous-like mechanisms in heterogeneous materials, which can achieve similar performance (e.g., chemical yield), while also being highly recyclable and robust due to the nature of the support. For instance, Pérez-Ramírez and co-workers demonstrated that Pd single-atoms dispersed on exfoliated carbon nitride exhibit superior performance, compared to state-of-the-art homogeneous catalysts for Suzuki coupling, thanks to the robustness and stability of this material.^[3] Similarly, some SACs undergo chemical reactions via mechanisms similar to biological systems and enzymes.^[4] In this sense, cytochrome P450 enzymes are involved in the oxidation of aromatic hydrocarbons to water-soluble metabolites.^[5] These enzymes contain iron atoms coordinated to porphyrin rings as active sites, which react with molecular oxygen (O₂) to produce highly reactive iron-oxo intermediates (Fe=O). Recent advances in the synthesis of metal SACs enabled the generation of such species in heterogeneous supports, such as graphene or N-doped carbons.^[4a,b] Our group recently reported the stabilization of iron single-atoms in poly(heptazine imide) (PHI) by a simple cation exchange method.^[6] This material offers numerous advantages, including the abundance of carbon and nitrogen as support elements, as well as highly reproducible and controlled metal loading for single-atom coordination.^[6] This is in contrast to N-doped carbon materials and graphene, which lack the same level of reproducibility and controlled metal loading for single-atom coordination. The lack of reproducibility and poor control over metal loading in such materials can be attributed to the variance or absence of metal anchoring points, which limits the precision of grafting single metals at desired positions. Also, the cation exchange method has proven to be very versatile since it can be employed for a wide variety of metals.^[7] For example, copper and nickel can be coordinated onto PHI structures, and other elements can be stabilized as well.^[7c,d] Notably, non-noble metals such as Mn and Fe exhibit similar behavior in various oxidation reactions of C–H bonds in nature.^[8] The production of metal single-atoms based on iron and manganese focusing on C–H oxidation reaction is therefore quite relevant.

Recently, some evidence has been found suggesting that iron oxo groups may be the reactive species responsible for the selective oxidation of hydrocarbons using Fe-PHI photocatalysts.^[6] In the present study, we synthesized SACs of both Fe and Mn on the PHI structure by a cation exchange method and demonstrated their high selectivity for C–H photooxidation in alkylaromatics

and benzyl alcohols to aldehydes, which are crucial compounds for the chemical industry. Our data indicate that the high selectivity observed is owing to the formation of iron and manganese oxo species, which are photogenerated by the oxidation of the metal center in a reversible fashion. Furthermore, the reaction does not involve any reactive free radicals, a key property to drive the selectivity toward aldehydes. These results are of great significance, as they pave the way to elucidate the mechanism behind SACs and their close relationship to homogeneous metal complexes or enzymes.

2. Results and Discussion

2.1. Catalyst Characterization

Poly(heptazine imide) materials are widely employed photocatalysts,^[7a,c,d,9] and the process to introduce transition metals within their structures by an aqueous cation exchange has been previously described in some reports from our group.^[6,7b-d,9e] This same method was applied in the present work (Figure S1, Supporting Information), and, for the first time, successfully employed to synthesize manganese-based single-atom catalysts. The X-ray diffraction (XRD) patterns and fast Fourier transforms (FFTs) obtained from high-resolution transmission electron microscopy (TEM) and bright-field scanning transmission electron microscopy (STEM) images were indexed in a hexagonal lattice, space group *P31m*, similar to previously reported PHIs.^[10] The structure's integrity is mostly preserved after the addition of metals, as shown in Figure 1a,b. A narrow intense (100) peak at 8° on the XRD pattern of Na-PHI is related to the heptazine units repeating throughout the framework; a set of several overlapping reflections with maximum position at ≈27° corresponds to the (001) plane in the structure that relates to the distance between heptazine layers.^[7a,11] The distributions of intensities and shapes of peaks on XRD patterns of Fe-PHI and Mn-PHI are slightly different from those on the pattern of Na-PHI, indicating possible distortion of the lattices because of metal exchange. These features can also be associated to ordering loss caused by turbostratic disorder, which is mostly pronounced at higher metal loading, probably due to the large volume of metals inserted in the spacing between the heptazines.^[6]

Vibrational spectra were recorded for the pristine Na-PHI and the corresponding Fe-PHI and Mn-PHI (1% of metal loading

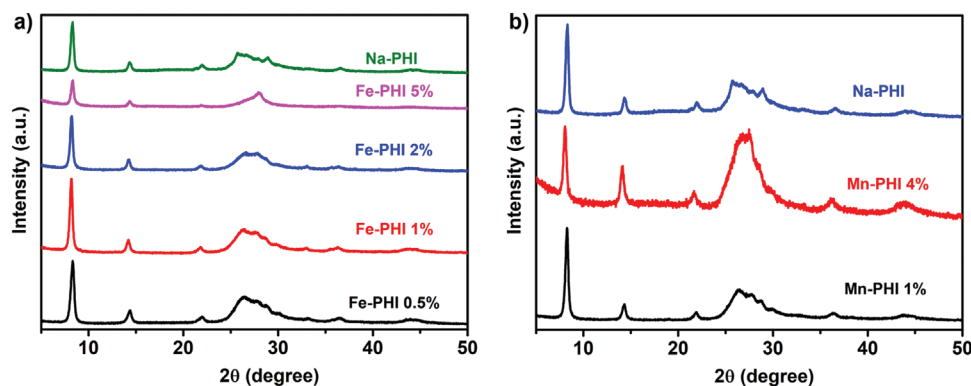


Figure 1. XRD patterns of: a) Fe-PHI and b) Mn-PHI materials with different metal loadings compared with pristine Na-PHI.

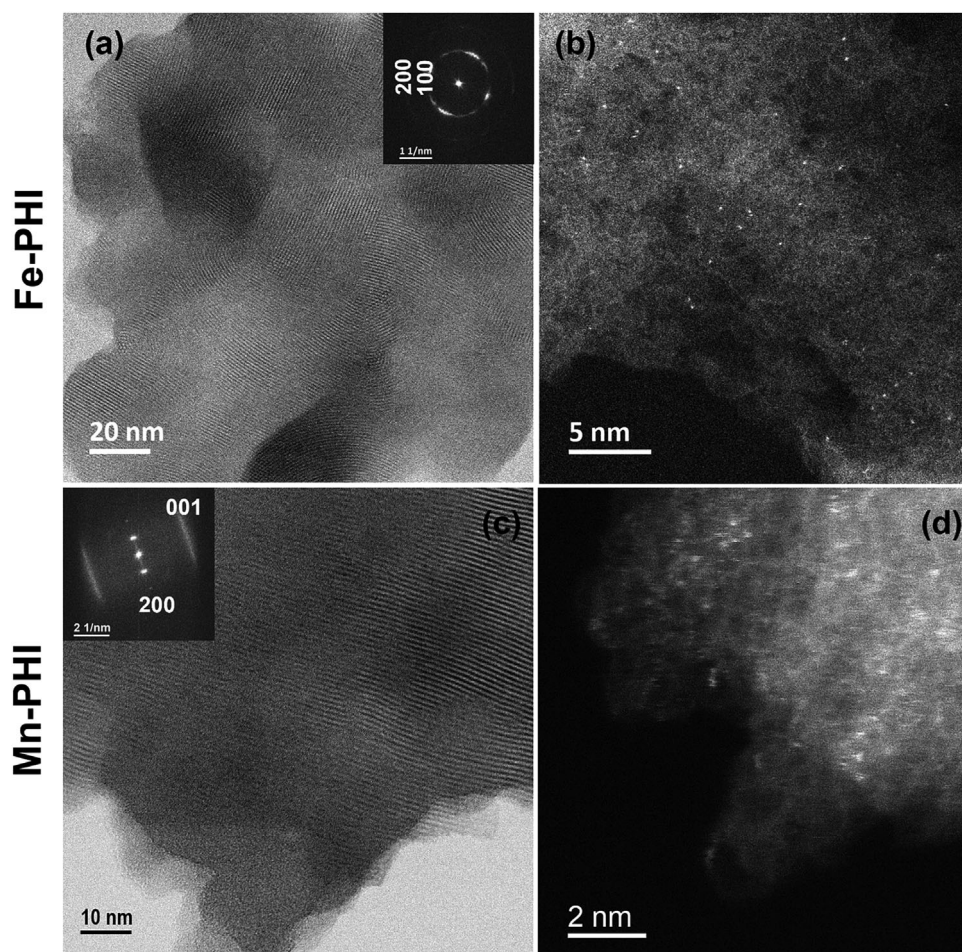


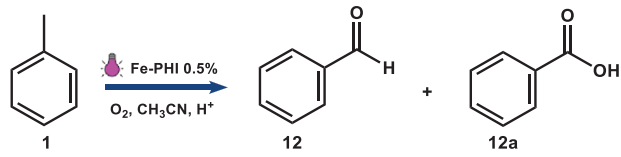
Figure 2. a,c) BF-STEM images of Fe-PHI and Mn-PHI and the corresponding FFT patterns in insets. FFTs are indexed using a hexagonal unit cell, typical for PHI structures.^[6,7a,10] b,d) HAADF-STEM images of Fe-PHI and Mn-PHI showing isolated metal atoms as bright dots on the lower-contrast carbon-nitride matrix.

each) to understand the chemical composition of such materials. Raman spectra of Na-PHI, Fe-PHI, and Mn-PHI (Figure S2, Supporting Information) show typical bands from poly(heptazine imide) structures. The main band at 733 cm^{-1} is assigned to the breathing modes of heptazine units.^[6] Also, the bands around 800 and 658 cm^{-1} are related to C–N vibrations. Moreover, vibrations of N–C=N bonds can be identified in the 950 – 1280 cm^{-1} region. All the Raman wavenumbers and their corresponding vibrations are listed in Table S1 (Supporting Information).^[7c,12] FT-IR spectra of Fe-PHI and Mn-PHI (Figure S3, Supporting Information) display a very similar binding structure compared to Na-PHI, where it is possible to point out the presence of a broad absorption band at 3500 – 3000 cm^{-1} , due to the hydroxyl groups stretching modes from adsorbed water and residual primary (H_2NC) and secondary (HNC_2) amino groups on the surface of the structure. Furthermore, it is possible to identify the presence of cyano and cyanamide groups vibrational bands at $\approx 2180\text{ cm}^{-1}$ due to C \equiv N stretch.^[13] The bands at 1640 and 1570 cm^{-1} are due to N–H stretching of amino groups. Characteristic signals in the 1450 – 800 cm^{-1} range relate to heteroaromatic ring systems, corresponding to C–N and N–C=N stretching and bending vibrations modes.^[9c,14] In all samples, two different bands can be

assigned at 990 and 910 cm^{-1} . These bands are associated with the presence of metals in the PHI scaffold, anchored through the electron-rich nitrogen bridge (M–NC_2 ; M = metal). The persistence of these bands after the ion exchange process is a strong indication of the introduction of metal in the polymeric structure. The metals incorporated into the PHI structure appear to adopt the same oxidation state as the chloride precursors. In the case of Fe-PHI, for instance, trivalent ions are the predominant species in the catalyst, as evidenced by XPS analysis (Figure S4, Supporting Information). Similar findings are observed in X-ray absorption spectroscopy (XAS) analysis for both Fe-PHI and Mn-PHI materials, which will be further explained later.

Scanning transmission electron microscopy (STEM) analyses show that all compounds consist of large, flat, μm -sized flakes (Figure S5, Supporting Information). High-resolution bright-field (BF) STEM images indicate that these flakes comprise domains $\approx 30\text{ nm}$ in diameter (Figure 2a,c). Both BF-STEM images and FFT patterns confirm that the crystal structure within the domains is not perfect, but displays considerable disorder, in particular stacking faults and rotational domains. The presence of planar defects corresponds well with the changes in shape and intensities of the peaks on the XRD patterns of Fe- and

Table 1. Photocatalytic toluene oxidation by using Fe-PHI as catalyst.



Entry	Catalyst [mg]	Additive	Conversion [%]	Selectivity [%]		TON
				12	12a	
1	Fe-PHI (50 mg)	–	96	92	8	40.3
2	Na-PHI (50 mg)	–	80	14	54	–
3 ^{a)}	Fe-PHI (50 mg)	–	5	60	40	2.1
4	Fe-PHI (25 mg)	–	46	98	2	38.6
5 ^{b)}	Fe-PHI (25 mg)	–	32	96	4	26.9
6	Fe-PHI (25 mg)	TBA	42	95	5	35.3
7	Fe-PHI (25 mg)	IPA	67	90	10	56.3
8	Fe-PHI (25 mg)	EDTA	72	91	9	60.5
9	Fe-PHI (25 mg)	Sodium Oxalate	80	96	4	67.2
10	Fe-PHI (25 mg)	PPh ₃	4	100	–	3.4
11	Fe-PHI (25 mg)	BQ	47	90	10	39.5

Reaction Conditions: Toluene (188 μ mol), CH₃CN (3 mL), O₂ (1 bar), H₂SO₄ (10 μ L), 20 h irradiation at 410 nm (100 W); Additives concentration: 0.25 m; ^{a)} No light; ^{b)} Air as oxidant. TBA: *tert*-butanol; IPA: isopropanol; BQ: 1,4-benzoquinone.

Mn-containing PHIs. High-angle annular dark-field (HAADF) STEM images of both Fe-PHI and Mn-PHI show bright spots, which are clearly visible on thin areas of the PHI flakes and correspond to metal atoms. Thus, iron single-atoms can coordinate with nitrogen atoms present in the poly(heptazine imide) heterocycles. The presence of tetracoordinated Fe–N₄ species was revealed with extended X-ray absorption fine structure (EXAFS), which also excluded the presence of Fe–Fe bonds.^[6]

The high crystallinity and organization of these materials enable a fine control of metal loading, promoting the formation of a single-atom catalyst (SAC) with a controlled metal addition system. Tables S2 and S3 (Supporting Information) show the correlation between the amount of metal chloride added and the quantified metal loading on the resulting PHI compound. For Fe-PHI, for example, different concentrations of iron chloride were inserted to produce metal loadings (w/w%) of 0.1%, 0.5%, 1%, 2%, and 4% (Table S2, Supporting Information). The same trend is observed for the manganese samples, as shown in Table S3 (Supporting Information).

2.2. C(sp³)–H Photooxidation Tests in Alkylaromatics

Photooxidation of C(sp³)–H bonds in the presence of the prepared photocatalysts were evaluated using toluene (1) as model substrate and molecular oxygen (O₂) as terminal oxidant. The reactions were carried out in acidic (by H₂SO₄) acetonitrile by using a 410 nm LED as the irradiation source (see Tables 1 and 2 and Experimental Section for further details). The results observed for both Fe-PHI and Mn-PHI indicate that toluene is selectively oxidized toward benzaldehyde. Fe-PHI exhibits higher toluene conversions when Fe content is below 2%, which

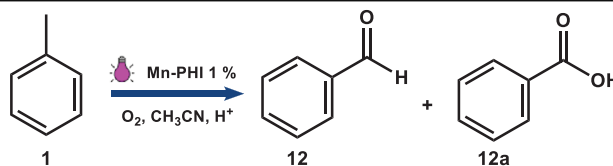
is in agreement with single-atoms predominance for low iron loadings (Figure 3a).

In all reactions, only benzaldehyde (12) and benzoic acid (12a) were identified as products, with a high selectivity toward benzaldehyde for all the Fe-PHI photocatalysts (Table 1). The selectivity does not seem to change for these materials, showing results above 90% for all the photocatalysts. This is clear reflection that benzaldehyde is formed in the primary visit of toluene to the surface, as the selectivity is preserved at different toluene conversion values (Figure 3b).

In this system, Fe-PHI 0.5% (50 mg) is the best catalyst for benzaldehyde production, with 96% conversion and 92% selectivity (Figure 3a,b and Entry 1, Table 1). On the other hand, Na-PHI exhibits a high conversion but poor selectivity (Entry 2), mainly due to the formation of CO₂, as determined by GC-BID, and significant amounts of benzoic acid. The light irradiation is crucial for toluene conversion as shown in Entry 3. Similarly, lowering the amount of catalyst only affects the conversion extent, while the selectivity to benzaldehyde remains excellent (Entry 4). Also, when air is used in place of molecular oxygen, the aldehyde production is still relevant, showing the ability of the photocatalyst to exploit an inexpensive oxidant source (Entry 5).

For manganese photocatalysts, Mn-PHI 1% exhibits the highest benzaldehyde yield (with 86% conversion and 90% selectivity) upon irradiation at 410 nm (10 W) for 12 h (Figure 3c and Table 2, Entry 1). The progression of benzaldehyde formation along with reaction time follows the same trend observed for iron, with a slight decrease in selectivity at long reaction times (Figure 3d). Also, no reaction occurs without light irradiation (Table 2, Entry 2). Moreover, Na-PHI exhibits a high conversion but lower selectivity, with a strong production of CO₂ (Table 2, Entry 3).

Table 2. Photocatalytic toluene oxidation reaction by using Mn-PHI 1% as catalyst.



Entry	Catalyst [mg]	Additive	Conversion [%]	Selectivity [%]		TON
				12	12a	
1	Mn-PHI (20 mg)	–	86	90	10	11.1
2 ^{a)}	Mn-PHI (20 mg)	–	2	99	1	0.3
3	Na-PHI (20 mg)	–	97 ^{d)}	12	40	–
4 ^{b)}	Mn-PHI (20 mg)	–	42	95	5	5.4
5	Mn-PHI (20 mg)	TBA	95	91	9	12.3
6	Mn-PHI (20 mg)	IPA	85	88	12	11.0
7	Mn-PHI (20 mg)	EDTA	97	88	12	12.5
8 ^{b)}	Mn-PHI (20 mg)	H ₂ O ₂	64	94	6	8.3
9 ^{c)}	Mn-PHI (20 mg)	–	7	91	9	0.9

Reaction Conditions: Toluene (47 μmol), CH₃CN (1 mL), O₂ balloon, H₂SO₄ (2.5 μL), 12 h; Additives concentration: 0.25 m. ^{a)} No light; ^{b)} 5 h; ^{c)} Without H₂SO₄; ^{d)} CO₂ Selectivity (48%). TBA: *tert*-butanol; IPA: isopropanol.

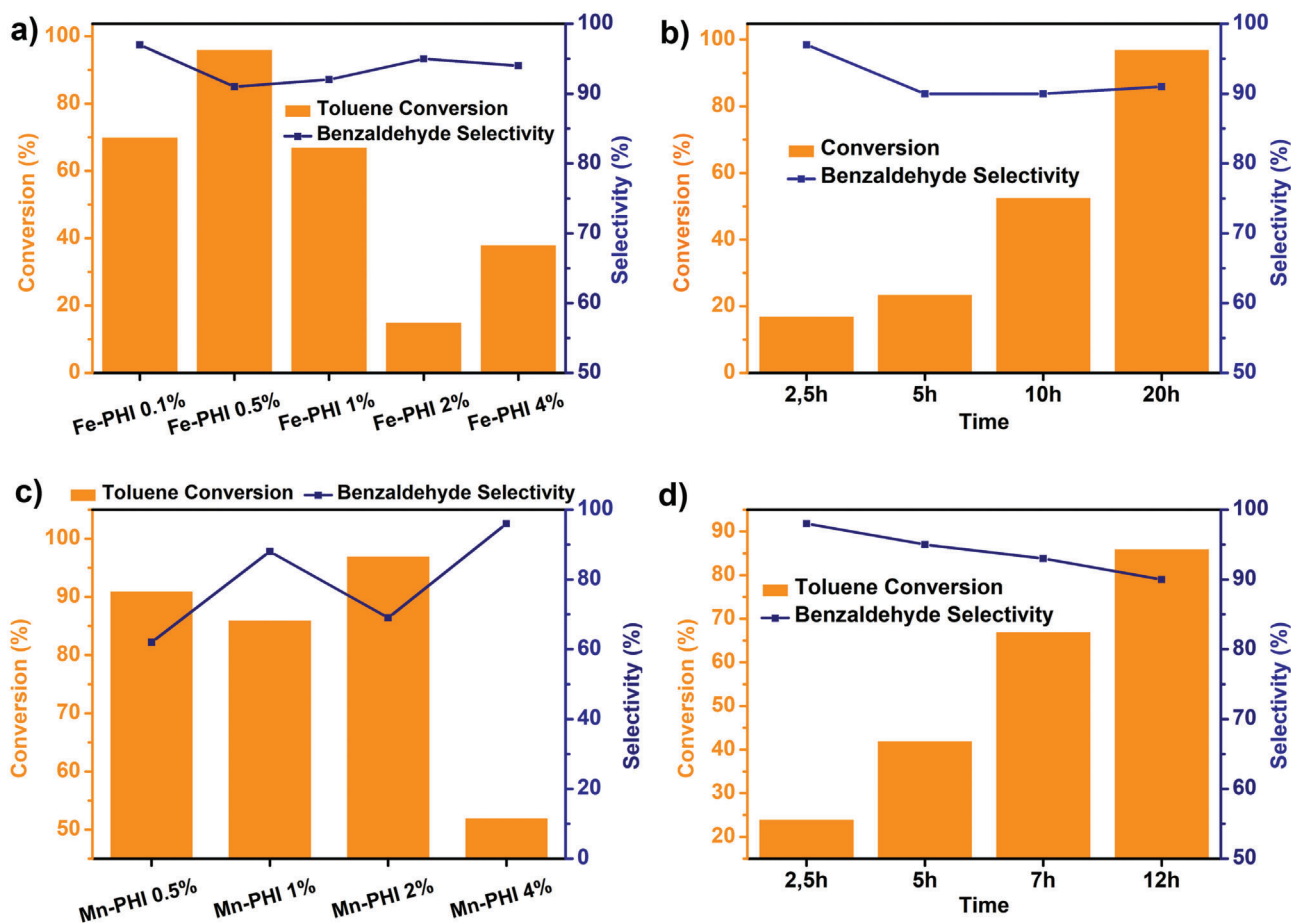


Figure 3. Toluene photooxidation results for different loadings of: a) Fe-PHI and c) Mn-PHI. Evolution of toluene conversion and selectivity to benzaldehyde along reaction time for: b) Fe-PHI 0.5% and d) Mn-PHI 1%. Reaction conditions for Fe-PHI: irradiation at 410 nm (100 W) for 20 h, except where otherwise noted; reaction conditions for Mn-PHI: irradiation at 410 nm (10 W) for 12 h, except where otherwise noted.

The versatility of these photocatalysts for C(sp³)–H oxidation was investigated using substrates with different substituents on the aromatic ring (1–11). As depicted in Table 3, a wide range of structures can undergo benzylic oxidation to the corresponding aldehydes (e.g., products 12–14 as representative examples), quite independently of the substituents nature present. Benzaldehyde was selectively formed from 1 in a satisfying yield (61%), even when performing the reaction on a 3.76 mmol scale (20-fold scale up). Terephthalaldehyde 15 is the sole product arising from the oxidation of *p*-xylene 4. Notably, when an ethyl group is present (e.g. in 4-ethyltoluene 5), the CH₂ unit is preferentially oxidized over the CH₃ group, resulting in the formation of ketone 16 as the primary product at short irradiation times (15 h). On the other hand, product 17 is obtained at longer irradiation times (24 h), demonstrating the photocatalyst's ability to forge two different carbonyl moieties within the same molecule. Importantly, this substrate indicates that the selectivity in terms of product formation can be controlled kinetically. Application of the oxidation protocol catalyzed by Fe-PHI to 4-vinyltoluene (6) enables to obtain products 18 (15 h) or 15 (24 h) in a highly selective fashion, depending on the irradiation time. When using 4-methylbenzyl alcohol (7) as the substrate and Mn-PHI as the catalyst, the corresponding aldehyde 19 (15 h irradiation) is the sole product, indicating that the CH₂–OH moiety is oxidized to aldehyde more rapidly than the CH₃ group. Noteworthy, no competitive overoxidation into the corresponding benzoic acid took place. However, the methyl substituent in 7 can be oxidized as well into a formyl group by prolonged irradiation (24 h) to give 15 in 71% yield. These results highlight the broad applicability of these materials, where kinetic control can be employed to oxidize selectively different substrates toward aldehydes in a single step.

2.3. Benzylic Alcohols and Sulfides/Thiols Photooxidation Tests

The outcome of the oxidation of 4-methylbenzyl alcohol (7) led to the interesting discovery that benzylic alcohols may also be converted into benzaldehydes. Additional experiments on these substrates demonstrate that the parent benzyl alcohol (8) exhibits an exceptional selectivity, producing benzaldehyde in a remarkable yield (97%) in just 7 h when using the Mn-PHI catalyst. This further demonstrates the high selectivity of this material. Moreover, the production of aldehydes extends to other substituted benzyl alcohols (9–11) as illustrated in Table 3, where only the presence of strong electron-withdrawing groups (e.g., a nitro group in alcohol 11) has deleterious effects on the oxidation yield (ca. 40% for 21). It is worth noting that the conversion of benzyl alcohol to benzaldehyde occurs much more rapidly compared to that of toluene, as apparent from Figure S6 (Supporting Information).

Taking into consideration the ability of iron- and manganese-PHI catalysts to selectively oxidize C–H bonds, we further explored their applicability to sulfur oxidation in sulfides/thiols (Table 3). Interestingly, the photooxidation tests with sulfur-containing substrates (22, 24) resulted in highly selective conversions in a substrate-dependent fashion. For instance, dimethyl sulfide was transformed into dimethyl sulfoxide 23 after 15 h of irradiation in the presence of Mn-PHI with no competitive formation of dimethyl sulfone. In contrast, the oxidation of thio-phenol (24) yielded strong benzenesulfonic acid 25 in 95% yield.

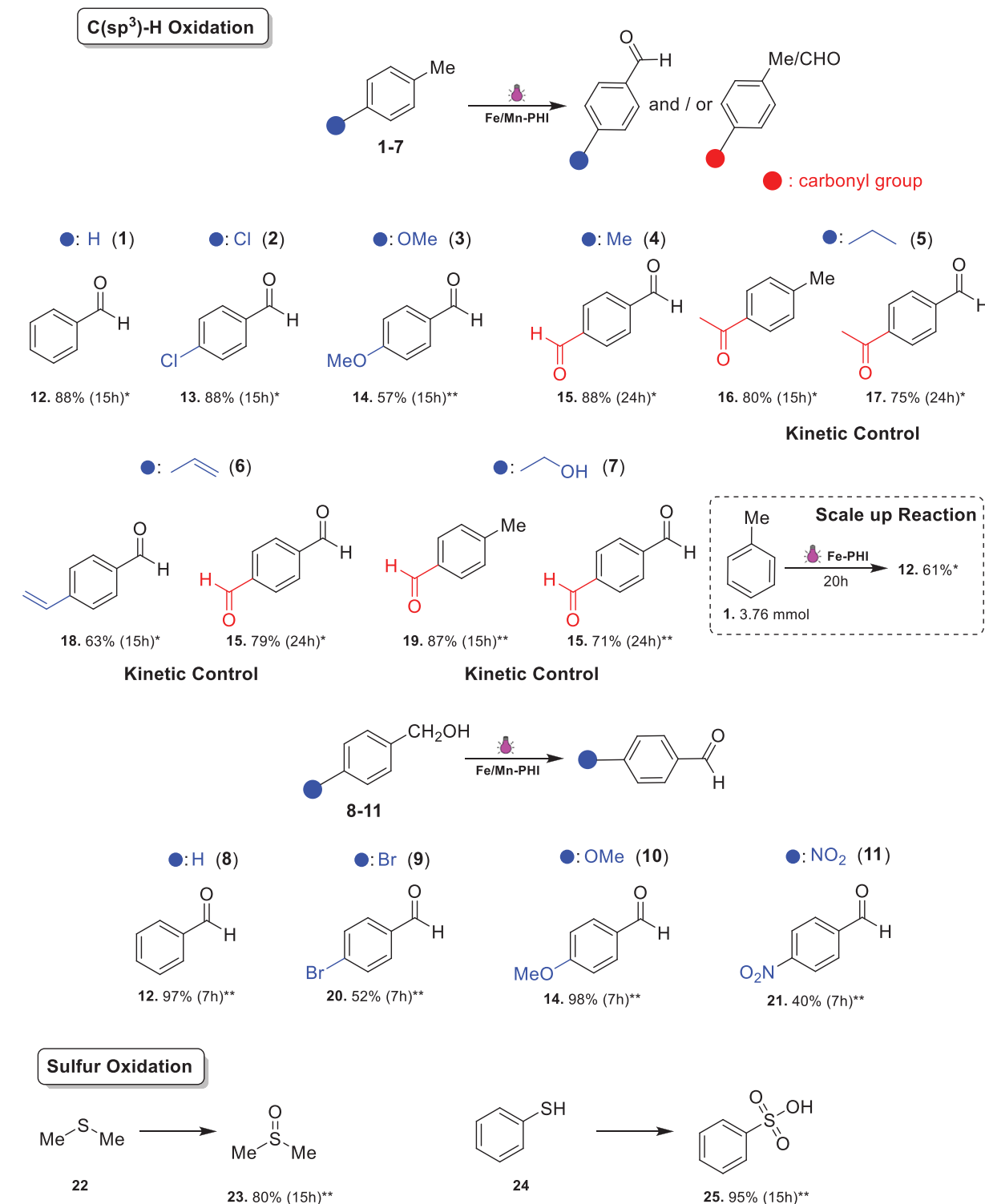
These findings underscore the broad versatility of Fe-PHI and Mn-PHI catalysts in photooxidation reactions, which occur under mild conditions utilizing O₂ as the oxidant.

2.4. Scavenger Assays

In a heterogeneous photocatalytic reaction, the effective separation of electron–hole pairs within the semiconductor plays a crucial role in facilitating reductive and oxidative reactions. Thus, to discern the prominent species involved in this reaction, scavenger tests were conducted. The results obtained indicate that Fe-PHI and Mn-PHI catalysts exhibit similar behavior for toluene oxidation, as evidenced by comparable outcomes when scavengers are introduced. As can be seen from Table 1 (compare Entries 4 and 6) and Table 2 (compare Entries 1 and 5), *tert*-butanol (TBA; a radical scavenger) did not affect the overall yield of benzaldehyde. However, isopropanol (IPA, a hole scavenger) seems to improve the catalytic activity (Table 1, Entry 7). The same trend is observed when sodium oxalate and EDTA were used as hole scavengers (Table 1, Entries 8 and 9 and Table 2, Entry 7). Such result appears to be contradictory to the idea of toluene oxidation by photogenerated holes and stands in contrast with previous works where holes play an important role to determine the photocatalytic activity of Fe-PHI.^[6] This apparent anomaly is also observed for Mn-PHI. To further investigate this effect, controlled amounts of IPA were introduced in the reaction system. As can be seen from Figure S7 (Supporting Information), when IPA concentration rises from 0.25 to 1 M, there is a decrease of the reaction yield performed with Mn-PHI, showing that, at higher concentrations of hole scavenger, the activity of the photocatalyst is lower than without scavenger. This feature is in agreement with previous works that pointed out the relevance of photogenerated holes in selective oxidation.^[6] However, the rise in the activity with 0.25 M of IPA is still intriguing and we propose that IPA acts as promoter of H₂O₂ generation (from O₂) by a fast hole quenching, i.e., IPA is first oxidized leading to the accumulation of electrons in the conduction band, which are able to produce H₂O₂. This step avoids the premature oxidation of toluene by holes, when low amounts of peroxide are present in solution. At higher concentrations of IPA, this compound competes for the holes, which are not directly responsible for the selective oxidation of toluene to benzaldehyde, but are essential to promote the formation of M=O groups. To test this idea, small amounts of H₂O₂ (along with oxygen) were added prior to the reaction, whereby a significant increase in the selectivity and conversion were observed with Mn-PHI after 5 h of reaction (Table 2, Entry 8; Figure S8, Supporting Information). Therefore, small concentrations of hole scavenger are beneficial to induce hydrogen peroxide production and avoid the direct oxidation of toluene promoted by holes. On the other hand, high concentrations of hole scavengers might compete for the active sites or disfavor the formation of metal oxo groups, negatively affecting the reaction.

Metal atoms clearly play a pivotal role in this reaction and, to probe their importance, triphenylphosphine was introduced into the reaction to coordinate Fe sites in Fe-PHI and prevent them to interact with the substrate (Figure S9, Supporting Information).^[15] This poisoning study reveals that, after the addition of PPh₃, the activity of the photocatalyst decreases

Table 3. Substrate scope for photocatalytic oxidation using Fe-PHI (*) and Mn-PHI (**).



Reaction Conditions: **Fe-PHI** (*): Substrate (188 μ mol), Fe-PHI (0.5%, 50 mg), CH₃CN (3 mL), O₂ balloon (1 bar), H₂SO₄ (10 μ L), irradiation at 410 nm (100 W); **Mn-PHI** (**): Substrate (47 μ mol), Mn-PHI (1%, 20 mg), CH₃CN (1 mL), O₂ balloon (1 bar), H₂SO₄ (2.5 μ L), irradiation at 410 nm (10 W). Scale-up experiment: 3.76 mmol Toluene, catalyst (1 g), CH₃CN (60 mL), H₂SO₄ (0.2 mL), irradiation at 410 nm (100 W) for 20 h, 1 bar O₂.

dramatically (Table 1, Entry 10), indicating that iron sites are crucial for toluene conversion.

2.5. Mechanism Investigation of Fe-PHI and Mn-PHI

To elucidate the role of metal-oxo groups, a series of experiments were conducted to investigate their reactivity. Initially, to ascertain whether C–H bond dissociation in toluene serves as the rate-determining step of the reaction, photocatalytic tests were performed using toluene- d_8 . The inclusion of deuterium atoms resulted in slower reaction kinetics, as illustrated in Figure S10 (Supporting Information), with a kinetic isotope effect (KIE) of 1.8. Furthermore, the mass spectrum of benzaldehyde (Figure S11, Supporting Information) obtained after the reaction confirmed the exclusive presence of deuterium in the product. This indicates that, despite the introduction of H^+ species, they are not retained in the final product. In other words, the acid does not act as a proton source during product formation.

To investigate the formation of radical species in the system, EPR experiments were performed in O_2 -saturated acetonitrile in the presence of the spin trap 5,5-dimethyl-1-pyrroline-*N*-oxide (DMPO). Under neutral conditions, the spin trapping measurements revealed that Fe-PHI can produce the superoxide anion (Figure S12a, Supporting Information). The spin adduct of this reactive oxygen species has a characteristic four-line spectrum and the observed line broadening is caused by the interactions between the unpaired electron of DMPO- O_2 radical and molecular oxygen in the reaction medium.^[16] However, a surprising feature is observed under acidic conditions, where no signal of radicals is observed (Figure S12b, Supporting Information). This result suggests that superoxide radicals are not produced when acid is introduced. However, the activity is highly improved with the addition of sulfuric acid (Table 2, Entry 9). Thus, we can propose that superoxide radicals are not involved in the catalytic cycle. This idea is corroborated by the addition of 1,4-benzoquinone (BQ; a superoxide radical scavenger) to the reaction mixture, which did not affect the overall reaction yield (Table 1, Entry 11).

Under neutral conditions and when using toluene as substrate, a spin adduct with the hydrogen hyperfine splitting constant larger than that of nitrogen was detected, even in an argon atmosphere (Figure S13, Supporting Information, $a_N = 14.7$ G and $a_H = 20.1$ G). This type of spectrum can be related to C-

centered radicals^[17] and, since toluene was added as the substrate in the system, such spin adduct can be assigned as the reaction product generated from DMPO and $PhCH_2^\bullet$ radicals. As the system has no O_2 acting as an electron scavenger, the signal of the delocalized electron of carbon nitride ($g \approx 2.00$)^[6,18] increased significantly during the measurement. By using the Easyspin simulation software, it was possible to deconvolute the hidden transition line of DMPO spin adduct from Fe-PHI signal. This result indicates that, without the acid additive, superoxide and benzyl radicals are produced by Fe-PHI. Nevertheless, the yield of benzaldehyde is extremely low under these conditions. In fact, CO_2 is detected under neutral conditions, suggesting that radical formation leads to the mineralization of toluene instead of selective oxidation.

Since under acidic conditions we obtained the best results and no detectable free radicals were produced, we can conclude that these intermediates are not involved in the highly selective benzaldehyde generation by Fe-PHI. However, photogenerated electrons and holes are still produced by the semiconductor and are crucial toward the desired reactivity, since the reaction does not proceed without light (Table 1, Entry 3). Fe-PHI is known to produce hydrogen peroxide (H_2O_2) from O_2 , in a $2e^-$ reduction promoted by photogenerated electrons.^[6] Irradiating Fe-PHI in the presence of O_2 yields H_2O_2 under acidic conditions, as shown in Figure S14 (Supporting Information). Time-resolved photoluminescence (TR-PL) of Fe-PHI with hydrogen peroxide showed longer fluorescence lifetimes than pristine Fe-PHI (Table S4). This result can be explained by a hole quenching promoted by H_2O_2 .^[19] Thus, electrons in the conduction band react with O_2 to produce H_2O_2 , which participates in the quenching process of holes.

Photogenerated holes induce the iron sites oxidation into high-valent oxo species, which are active for oxidation reactions.^[6] To probe the oxidation state of Mn and Fe single site species supported in the PHI structure and changes thereof during the course of the reaction, operando X-ray absorption spectroscopy (XAS) experiments were performed for Fe-PHI and Mn-PHI in the presence of oxygen, oxygen and water, and upon light irradiation. Prior to the operando experiments, the sample was treated in flowing He at 250 °C, to remove all the possible water adsorbed. The corresponding XAS spectrum at the Fe $L_{2,3}$ edges is shown in Figure 4a and reshown in Figure 5a for better convenience.

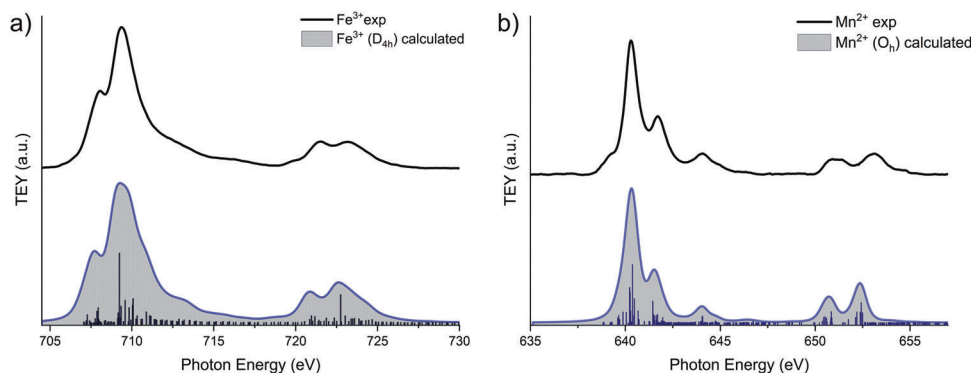


Figure 4. a,b) XAS spectra of L_3 and L_2 edges of: a) Fe-PHI and b) Mn-PHI.

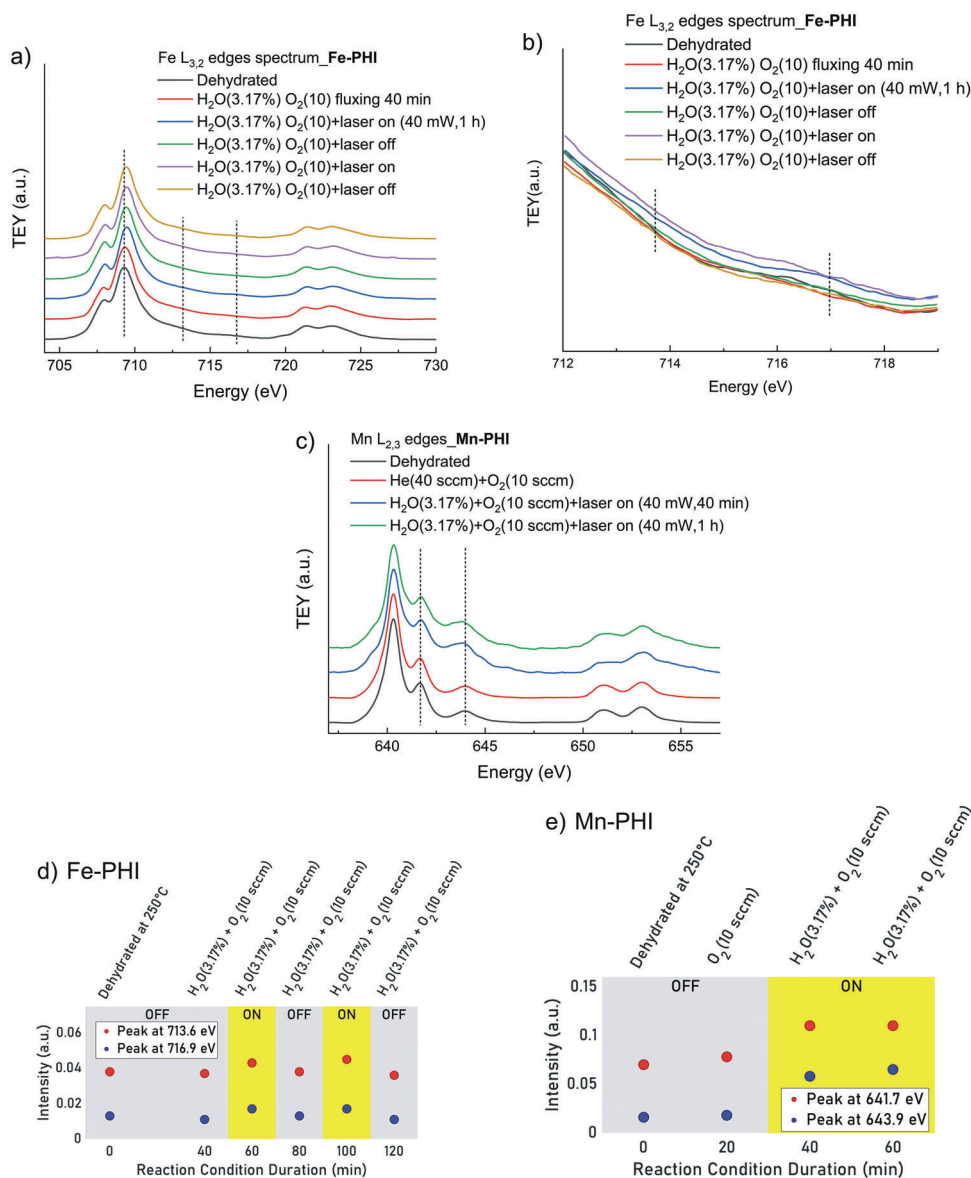


Figure 5. Operando XAS spectra at the Fe and Mn $L_{3,2}$ -edges of Fe-PHI and Mn-PHI. a) Spectra at the Fe $L_{3,2}$ -edges under different conditions; b) Enlargement of the high energy region of the Fe $L_{3,2}$ -edge under different conditions. c) Spectra at the Mn $L_{2,3}$ -edges under different conditions. Vertical dotted lines in (a)–(c) mark the spectral features of interest. d,e) Intensity of the high-energy peaks at the Fe (d) and Mn (e) $L_{3,2}$ -edges under different conditions. The yellow boxes highlight the period of illumination of the catalysts under the reaction conditions.

Comparison with standards and multiplet calculations demonstrate that Fe in these conditions is present mainly in the Fe(III) oxidation state (see Figure 4a). Operando experiments were then run at the same temperature (250 °C). Flowing only O_2 , a small decrease of the peak at *ca.* 708 eV is observed, coupled with a shift toward higher energies of the main peak at *ca.* 709.5 eV (Figure 5a; Figure S15, Supporting Information). Both features are indicative of further oxidation of iron species in Fe-PHI. Switching on the laser, and flowing a mixture of O_2 and H_2O , as described in the Experimental Methods, a more pronounced shift of the main peak toward higher energies is detected (Figure S15, Supporting Information), coupled with an increase of spectral weight in the 713–718 eV range, with the appearance of two

additional peaks in this region, which is shown on an enlarged scale in Figure 5b. This is clearly indicative that under these conditions the population of oxidized iron species increases, possibly with the formation of Fe in higher oxidation states. This result shows that light irradiation has a role in the promotion of the oxidation of iron sites into higher valent species, suggesting that photogenerated holes are interacting with iron sites and driving the formation of Fe=O species. This is confirmed by the fact that, after turning off the light, the main peak at *ca.* 709.5 eV shifts back to lower energies, and the peaks between 713 and 718 eV disappear (Figure S15, Supporting Information). For the sake of better clarity, the intensity at 713.6 and 716.8 eV is reported as a function of the different reaction conditions in Figure 5d. The

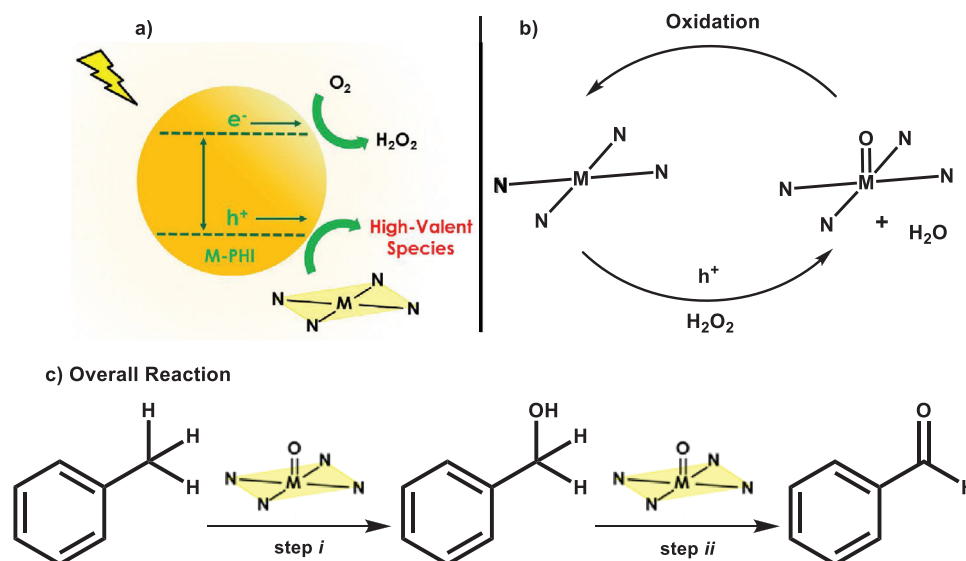


Figure 6. a) Photocatalytic mechanism of hydrogen peroxide and high-valent metal species formation. b) Mechanism of metal-oxo formation thanks to photogenerated holes and H_2O_2 . c) Proposed mechanism of toluene oxidation into benzaldehyde via benzyl alcohol, catalyzed by iron- and manganese-oxo species.

reversible behavior that is found in switching the laser on and off is well apparent. The process of turning the light on and off can be repeated, obtaining the same results (Figure S15, Supporting Information). A similar reversible behavior is observed at the L_2 edge.

The results obtained for the Mn-PHI catalyst at the Mn $L_{2,3}$ -edges indicate the same effect. The spectrum of the dehydrated catalyst at 250°C in flowing He is fully compatible with the presence of Mn(II) only (Figure 4b and Figure 5c). At this temperature, in the presence of O_2 , water, and under illumination, significant increase in the spectral weight in high-energy regions, i.e., between 640 and 645 eV, is detected (Figure 5c,e). Also, a clear shift toward higher energies for the main peak at ca. 640 eV is observed under these conditions. We point out that these changes are reversible as in the case of the Fe-PHI catalyst, and also evidence the formation of Mn in higher oxidation states, possibly Mn(IV). Overall, these results show that both iron and manganese atoms interact with holes to produce high-valent species.

In summary, the data obtained in this work indicate that the H_2O_2 produced in situ also behaves as an oxidant in these systems. These findings imply that both holes and hydrogen peroxide react with metal sites, yielding high-valence species (Figure 6a). These species are generally found in nature in cytochrome P450 enzymes, which possess metal-oxo groups ($\text{M}=\text{O}$) as active sites.^[5b,8a,20] Several works based on iron-complexes tried to mimic the active site of these enzymes, and, recently, the first evidences of iron-oxo species on heterogeneous supports were claimed.^[4a,b,6] Our data indicate that the oxidation reaction between hydrogen peroxide and iron centers produces iron-oxo groups in the Fe-PHI material. This feature can be inferred by a change of geometry observed from powder EPR in the presence of light. As stated above, the spectrum recorded in the absence of light displays a delocalized electron signal with $g \approx 2.00$, overlapped with Fe(III) high spin ions.^[21] However, it is also possible to observe some low-intensity anisotropic features

with $g \approx 2.01$, and such a signal increased when the light was switched on, reaching the maximum intensity after 5 min (Figure S16a, Supporting Information). The anisotropy behavior, as well as the evolution of those transition lines, corroborates the formation of Fe=O species since the bond between iron and oxygen modifies the geometry of these paramagnetic sites.^[22] Also, Raman analyses in the presence of H_2O_2 strongly indicate the formation of iron-oxo species by the appearance of a shoulder at 812 cm^{-1} (Figure S16b, Supporting Information).^[5b,6,23] A similar conclusion can be made for the Raman analysis of Mn-PHI in the presence of peroxide, whereby a small shoulder appears at 740 cm^{-1} , which could be related to Mn-oxo species (Figure S16c, Supporting Information).^[24]

Metal-oxo groups work as active centers for various oxidation reactions, and different mechanisms can be associated to these species. In our study, we observed similar behavior for iron and manganese, where photogenerated holes play a crucial role in the formation of high-valent metal species (Figure 6), as demonstrated by the operando XAS experiments under light irradiation (Figure 5), in which the presence of high-valent metal species was detected. In particular, in the case of Mn the increase of spectral weight in the region between 640 and 645 eV is safely assigned to Mn(IV) or even Mn(V) by comparison with literature data,^[25] and this is in perfect agreement with the formation of Mn=O species, as described in Figure 6b. In addition, a very recent paper has shown that the Fe $L_{2,3}$ -edge spectrum of Fe(IV) oxo compounds is characterized by an intense tail nearby the 715 eV energy range,^[26] which is closely matching the energy range where we detect the reversible increase of intensity (Figure 5b). In conclusion, all the spectral evidences at the Mn and Fe $L_{2,3}$ -edges support the formation of high valent-metal-oxo species.

Since different substrates are employed, we anticipate the involvement of distinct mechanisms. In the case of metal complexes, particularly in heme systems, the hydroxylation of C–H bonds commonly occurs through an initial C–H cleavage via

hydrogen atom transfer (HAT) followed by oxygen rebound.^[27] The occurrence of this peculiar mechanism can also explain the fact that no trappable free radical species can be detected in our EPR experiments (see Figure S12b, Supporting Information). Furthermore, the observed KIE (1.8) for toluene versus toluene-d8 oxidation (see Figure S10, Supporting Information) is similar to the values available in the literature for the oxidation of toluene by a manganese(IV)-oxo complex.^[28]

Indeed, while direct aldehyde production from hydrocarbons is less typical for oxo systems, it is known that aldehydes can be formed from alcohols.^[29] In line with our experimental findings, we have observed the selective production of benzaldehyde from benzyl alcohol, which occurs at a faster rate compared to toluene oxidation (Figure S6, Supporting Information). Based on this observation, we propose a two-step mechanism for benzaldehyde production from toluene (Figure 6c). First, benzyl alcohol is generated through the above-mentioned hydroxylation mechanism promoted by metal-oxo intermediates (step *i*). The formation of benzyl alcohol represents the slowest step, and this intermediate is then rapidly oxidized to benzaldehyde (step *ii*). This mechanism has been previously reported in related studies on alcohol oxidation.^[29]

Overall, these outcomes demonstrate that iron and manganese single-atoms are oxidized into high-valent oxo species during the reaction, which are highly active for C–H activation followed by C–O formation. Notably, the unique features of the adopted SACs enable the controlled oxidation of toluene, in contrast with literature reports describing the ultimate mineralization of this substrate.^[30] Also, the performance of the materials described here compares favorably with literature precedents,^[31] showing very high toluene conversion degrees and selectivity to benzaldehyde, with the added bonus of exploiting cheap and largely abundant elements.

These findings exemplify that SACs can pave new paths to replicate homogeneous-like mechanisms (see Figure 6) in heterogeneous systems, which are more stable and durable for large scale applications.

3. Conclusion

Iron and manganese metalloenzymes have been shown to be effective in C–H oxidations in nature, inspiring scientists to mimic their active sites in synthetic catalytic systems.^[32] In this work, we successfully employed a simple and versatile cation exchange method to synthesize Fe-PHI and Mn-PHI single-atoms photocatalysts, which were employed in the oxidation of several molecules such as hydrocarbons, alcohols, and sulfur-containing compounds. In the case of C–H bond photooxidation, the results obtained here show a remarkable selectivity toward aldehydes. This is not a trivial outcome, especially in the field of photocatalytic reactions, given that the production of reactive free radicals can induce over-oxidation of the products. Operando XAS evidences, together with the Raman and EPR data, allow to safely conclude that high-valent M=O species play a key role in the reaction mechanism, which proceeds in a way similar to metalloenzymes found in nature. These photocatalysts possess a unique oxidation mechanism in acidic media, without the production of reactive free radicals, which promotes the formation of iron and manganese oxo species commonly found in enzymes contain-

ing these metals. This work demonstrates the potential to utilize SACs to mimic homogeneous systems with greater robustness and stability.

4. Experimental Section

Cation Exchange Method (Mn-PHI and Fe-PHI Synthesis): The metals were anchored using a simple method of cation exchange in aqueous media developed by our group.^[6] Initially, a solution of each metal precursor (FeCl₃•6H₂O or MnCl₂•4H₂O) was prepared, whose concentration was dependent on the loading on the PHI structure (see Tables S2 and S3, Supporting Information). For the Fe-PHI containing 1% metal loading (w/w %), for instance, 5.4 mg of FeCl₃•6H₂O was dissolved in 2 mL of deionized water (DI) and added to 100 mg of Na-PHI. The mixture was sonicated for 30 min and washed several times with DI and dried at 60 °C overnight.

Photocatalytic Tests: Toluene photooxidation tests using Fe-PHI as catalyst were performed in a 50 mL quartz reactor with 410 nm LED (100 W) as the irradiation source (see Figure S17, Supporting Information, for the absorption edge of the photocatalyst and its estimated band structure). In each test, a known amount of the photocatalyst was dispersed in acetonitrile (3 mL) containing 0.188 mmol of the substrate, and 10 μL of H₂SO₄ and O₂ (1 bar). After the photocatalytic reaction, the catalyst was separated by centrifugation (10 000 RPM for 5 min), and the liquid phase was analyzed and the products quantified using GC-FID and GC-MS. The gaseous phase products were analyzed using GC-BID. Toluene photooxidation tests using Mn-PHI as catalyst were carried out in a 5 mL glass vial with 410 nm LED (10 W) as irradiation source. In each test, 20 mg of the photocatalyst was dispersed on acetonitrile (1 mL) along with 0.047 mmol of substrate, 2.5 μL of H₂SO₄, and an atmosphere of O₂ in a balloon. After the photocatalytic reaction, the catalyst was separated by centrifugation (10 000 RPM for 5 min), and the liquid phase was analyzed and the products quantified using GC-FID and GC-MS. The gaseous phase products were analyzed using GC-BID.

EPR Analyses: All the EPR data were obtained on a Bruker EMX CW-Micro X-band EPR spectrometer using a high-sensitivity resonator ER4119HS (with a grid in front side). The powder measurements were made in O₂ atmosphere, weighing 10 mg of Fe-PHI and placing it in a typical EPR quartz tube and then in the cavity, the in situ irradiation was performed using a 300 W Xe lamp equipped with a 395 nm cut-off filter. In general, for the spin trapping tests 5 mg of the catalyst, 10 mg of DMPO, and 1 mL of acetonitrile were added to a 1.5 mL vial and then an aliquot of this suspension was extracted using a 50 μL capillary, inserted in the tube and in situ irradiated. In some experiments the system was modified, adopting a different atmosphere (O₂ or Argon) and acidic conditions (H₂SO₄, 3.33 μL was added). All the spin-trapping spectra were simulated using Easyspin.^[33]

Characterization of the Catalysts: Powder X-ray diffraction (XRD) was acquired using a Bruker D8 Advance ECO with Cu-Kα1 (1.54 Å) emission and a scanning range between 5° and 50° (step of 0.02°). Fourier transform infrared (FT-IR) spectra were recorded on a Shimadzu IRSpirit spectrometer equipped with an attenuated total reflectance module containing a diamond prism, covering 400–4000 cm⁻¹ range at 2 cm⁻¹ of resolution. The Raman spectra were obtained using a Renishaw InVia Micro-Raman spectrometer (λ₀ = 785 nm from a diode laser) with an Olympus 80x objective. Measurements were performed in the range of 200–1200 cm⁻¹, 2 cm⁻¹ resolution with 1 accumulation and 20 s of exposure time. For the X-ray photoelectron spectroscopy (XPS) essays, the samples were prepared using carbon tape and were performed using a ThermoScientific Escalab 250 Xi applying a monochromated Al Kα X-ray source (1486.68 eV) micro-focused with a spot size of 400 nm. The binding energies were calibrated using LiCl. For scanning transmission electron microscopy (STEM) observations, a suspension of the sample in ethanol was sonicated for 10 min and then drop-casted to a Cu grid with a lacey carbon support and dried for 10 min. The STEM study was performed using a double Cs corrected JEOL JEM-ARM200F (S)TEM operated at 80 kV and equipped with a cold-field emission gun. High-angle annular dark-field scanning

transmission electron microscopy (HAADF-STEM) images were collected at a probe convergence semi-angle of 25 mrad. The “beam shower” procedure was performed for 30 min to reduce hydrocarbon contamination during subsequent imaging at high magnification.

XAS Experiments: For the operando XAS experiments, small amounts of the Fe-PHI and Mn-PHI photocatalysts (≈ 5 mg), in form of loose powder, were hand pressed on the sample holder of the reaction cell of the APE beamline at the ELETTRA synchrotron radiation facility. The sample holder was fixed with screws onto the titanium base of the cell, which was floating from ground and connected with a coaxial cable. In this geometry, the X-ray beam passes through a SiO₂ membrane and the gas layer, then hits the sample and generates the secondary emission, which was collected by a picoammeter connected to the sample and measuring the drain current. All the measurements were performed keeping the sample grounded through the picoammeter and applying a positive bias voltage of 50 V to the membrane. The cell was mounted in the ultra-high vacuum (UHV) chamber of the APE-HE beamline, coaxially with the X-ray beam.^[34] The reaction cell was mounted on an x-y table that allows its movement in the plane perpendicular to the incident beam with 5 μ m vectorial precision. This allows the alignment of the membrane on to the beam. The sample surface, inside the cell, sits in the focal point of the beamline. The measurements were performed at the Mn and Fe L_{2,3}-edges. Surface sensitivity was obtained by collecting the XAS spectra in total electron yield mode: the estimated probed depth was ca. 3–4 nm. The experiments were conducted in flowing He (40 standard cubic centimeter per minute, SCCM), either pure or with the addition of O₂ (2 SCCM), or O₂ (2 SCCM) plus a controlled amount of H₂O, which was flowed by using a bubbler, and by setting the water saturation pressure at 0.1 MPa. A 40 mW, 405 nm laser, impinging the sample via the transparent SiO₂ membrane, was used for the photochemical experiments. The spectra were calibrated in energy with respect to standard materials for the Mn and Fe L₃-edge. An absolute energy position was then obtained by comparison with literature data.^[35,36]

Multiplet calculations were performed by means of the CT4XAS code,^[37] using the following parameters: Mn²⁺ symmetry O_h, 10Dq = 0.2; Fe³⁺ symmetry D_{4h}, 10Dq = 2, Dt = 0.08, Ds = 0.2.

Multiplet Calculation: The L_{2,3}-edge X-ray absorption spectrum of 3d elements was dominated by dipole-allowed electron excitations from the 2p core states to the 3d valence states. In compounds of these elements, the 3d electrons were, in general, strongly affected by correlations, and, as an effect, localized. This means in turn that the 3d levels can be treated, with a good approximation, as nearly atomic levels. Thus, the near edge spectrum can be calculated simply by calculating all the probabilities of the transitions from the 3dⁿ initial state to the 2p⁵3dⁿ⁺¹ final state (3dⁿ → 2p⁵3dⁿ⁺¹).^[38] The calculations can be thought as performed in two steps. First, only the interactions within the absorbing atom were considered: the hole in the 2p states and the extra electron in the 3d state were strongly interacting, and this gives rise to a large number of final states (multiplets). Due to the very small core hole broadening at the 3d element L_{2,3}-edges, all these states were usually seen in the spectra.

Then, the effect of neighboring atoms was introduced as a perturbation, including crystal field and charge transfer effect.

Then, the program requires the following sets of parameters for the calculations: a) the electronic configuration of the 3d metal ion (number of 3d electrons in the initial state); b) all the crystal field parameters (i.e., 10Dq for octahedral symmetry, and the additional parameters Dt and Ds for lower symmetries); c) charge transfer parameters, accounting for possible covalence of the metal–ligand bonds; d) Slater integrals reduction parameters, which account for all the electron interactions (i.e., 3d electrons with each other, core state with valence state, etc.).

The program was semi-empirical: this means that parameters b,c were usually adjusted until a good correspondence between experiment and theory was obtained.

Mott–Schottky measurements: Mott–Schottky measurements were conducted utilizing a Biologic MPG-2 system with a three-electrode setup. This setup included a Pt wire serving as the counter electrode, an Ag/AgCl electrode as the reference electrode, and F-doped tin oxide (FTO) glass coated with the material acting as the working electrode. The FTO glass used for the working electrode was first cleaned through a 30 min sonica-

tion process in ethanol and then dried at 353 K. To protect the boundary of the FTO glass, Scotch tape was applied. Next, a 3 mg sample was dispersed in 0.2 mL of water through sonication, resulting in a slurry mixture to which 20 μ L of Nafion was added. This slurry was spread evenly onto the pre-treated FTO glass. After allowing it to air dry, the Scotch tape was removed, and the working electrode was further dried at 393 K for 2 h to enhance adhesion.

Supporting Information

Supporting Information is available from the Wiley Online Library or from the author.

Acknowledgements

This project received funding from the European Union’s Horizon Europe research and innovation program under grant agreement no. 101046836 (project acronym “CATART”). The publication reflects only the author’s views and the European Union is not liable for any use that may be made of the information content therein. S.S. acknowledges financial support by the CATART project via a Ph.D. grant. I.F.S. thanks the Alexander von Humboldt Foundation for their postdoctoral fellowship. This research was financially supported by the Brazilian funding agencies CAPES, CNPq (423196/2018-9, 403064/2021-0, and 405752/2022-9) and FAPESP (2020/14741-6, 2021/13271-9, 2022/16273-5, 2021/12394-0, 2021/13915-3 and 2021/11162-8). The authors are grateful to Ms. Bolortuya Badamdorj for the assistance with TEM characterization.

Conflict of Interest

The authors declare no conflict of interest.

Data Availability Statement

The data that support the findings of this study are available from the corresponding authors upon reasonable request.

Keywords

non-noble metals, photocatalysis, poly(heptazine imides), selective oxidation, single-atom catalysis

Received: May 4, 2023

Revised: September 15, 2023

Published online: November 20, 2023

- [1] a) G. F. S. R. Rocha, M. A. R. Da Silva, A. Rogolino, G. A. A. Diab, L. F. G. Noleto, M. Antonietti, I. F. Teixeira, *Chem. Soc. Rev.* **2023**, *52*, 4878; b) V. B. Saptal, V. Ruta, M. A. Bajada, G. Vilé, *Angew. Chem., Int. Ed.* **2023**, *62*, e202219306; c) S. K. Kaiser, Z. Chen, D. Faust Akl, S. Mitchell, J. Pérez-Ramírez, *Chem. Rev.* **2020**, *120*, 11703; d) S. Mitchell, E. Vorobyeva, J. Pérez-Ramírez, *Angew. Chem., Int. Ed.* **2018**, *57*, 15316; e) X.-F. Yang, A. Wang, B. Qiao, J. Li, J. Liu, T. Zhang, *Acc. Chem. Res.* **2013**, *46*, 1740; f) H. Zhang, G. Liu, L. Shi, J. Ye, *Adv. Energy Mater.* **2018**, *8*, 1701343.
- [2] a) F. Chen, X. Jiang, L. Zhang, R. Lang, B. Qiao, *Chin. J. Catal.* **2018**, *39*, 893; b) A. Iemhoff, M. Vennewald, R. Palkovits, *Angew. Chem., Int. Ed.* **2023**, *62*, e202212015.

- [3] Z. Chen, E. Vorobyeva, S. Mitchell, E. Fako, M. A. Ortuño, N. López, S. M. Collins, P. A. Midgley, S. Richard, G. Vilé, J. Pérez-Ramírez, *Nat. Nanotechnol.* **2018**, *13*, 702.
- [4] a) Y. Pan, Y. Chen, K. Wu, Z. Chen, S. Liu, X. Cao, W.-C. Cheong, T. Meng, J. Luo, L. Zheng, C. Liu, D. Wang, Q. Peng, J. Li, C. Chen, *Nat. Commun.* **2019**, *10*, 4290; b) D. Deng, X. Chen, L. Yu, X. Wu, Q. Liu, Y. Liu, H. Yang, H. Tian, Y. Hu, P. Du, R. Si, J. Wang, X. Cui, H. Li, J. Xiao, T. Xu, J. Deng, F. Yang, P. N. Duchesne, P. Zhang, J. Zhou, L. Sun, J. Li, X. Pan, X. Bao, *Sci. Adv.* **2015**, *1*, e1500462; c) L. Jiao, H. Yan, Y. Wu, W. Gu, C. Zhu, D. Du, Y. Lin, *Angew. Chem., Int. Ed.* **2020**, *59*, 2565.
- [5] a) I. G. Denisov, T. M. Makris, S. G. Sligar, I. Schlichting, *Chem. Rev.* **2005**, *105*, 2253; b) V. A. Larson, B. Battistella, K. Ray, N. Lehnert, W. Nam, *Nat. Rev. Chem.* **2020**, *4*, 404.
- [6] M. A. R. Da Silva, I. F. Silva, Q. Xue, B. T. W. Lo, N. V. Tarakina, B. N. Nunes, P. Adler, S. K. Sahoo, D. W. Bahnemann, N. López-Salas, A. Savateev, C. Ribeiro, T. D. Kühne, M. Antonietti, I. F. Teixeira, *Appl. Catal. B* **2022**, *304*, 120965.
- [7] a) A. Savateev, S. Pronkin, M. G. Willinger, M. Antonietti, D. Dontsova, *Chem. Asian J.* **2017**, *12*, 1517; b) F. M. Colombari, M. A. R. Da Silva, M. S. Homsy, B. R. L. De Souza, M. Araujo, J. L. Francisco, G. T. S. T. Da Silva, I. F. Silva, A. F. De Moura, I. F. Teixeira, *Faraday Discuss.* **2020**, *227*, 306; c) M. A. R. Da Silva, J. C. Gil, N. V. Tarakina, G. T. S. T. Silva, J. B. G. Filho, K. Krambrock, M. Antonietti, C. Ribeiro, I. F. Teixeira, *Chem. Commun.* **2022**, *58*, 7419; d) M. A. R. Da Silva, G. F. S. R. Rocha, G. A. A. Diab, C. S. Cunha, V. G. S. Pastana, I. F. Teixeira, *Chem. Eng. J.* **2023**, *460*, 141068.
- [8] a) K. P. Bryliakov, E. P. Talsi, *Coord. Chem. Rev.* **2014**, *276*, 73; b) M. Guo, T. Corona, K. Ray, W. Nam, *ACS Cent. Sci.* **2019**, *5*, 13.
- [9] a) Z. Chen, A. Savateev, S. Pronkin, V. Papaefthimiou, C. Wolff, M. G. Willinger, E. Willinger, D. Neher, M. Antonietti, D. Dontsova, *Adv. Mater.* **2017**, *29*, 1700555; b) A. Ausavasukhi, Y. Huang, A. T. To, T. Sooknoi, D. E. Resasco, *J. Catal.* **2012**, *290*, 90; c) A. Savateev, D. Dontsova, B. Kurpil, M. Antonietti, *J. Catal.* **2017**, *350*, 203; d) A. Savateev, S. Pronkin, J. D. Epping, M. G. Willinger, C. Wolff, D. Neher, M. Antonietti, D. Dontsova, *ChemCatChem* **2017**, *9*, 167; e) A. Rogolino, I. F. Silva, N. V. Tarakina, M. A. R. Da Silva, G. F. S. R. Rocha, M. Antonietti, I. F. Teixeira, *ACS Appl. Mater. Interfaces* **2022**, *14*, 49820; f) I. F. Teixeira, N. V. Tarakina, I. F. Silva, N. López-Salas, A. Savateev, M. Antonietti, *Adv. Sustain. Syst.* **2022**, *6*, 2100429; g) S. K. Sahoo, I. F. Teixeira, A. Naik, J. Heske, D. Cruz, M. Antonietti, A. Savateev, T. D. Kühne, *J. Phys. Chem. C* **2021**, *125*, 13749.
- [10] A. Savateev, N. V. Tarakina, V. Strauss, T. Hussain, K. Ten Brummelhuus, J. M. Sánchez Vellido, Y. Markushyna, S. Mazzanti, A. P. Tyutyunnik, R. Walczak, M. Oschatz, D. M. Guldi, A. Karton, M. Antonietti, *Angew. Chem., Int. Ed.* **2020**, *59*, 15061.
- [11] I. F. Teixeira, N. V. Tarakina, I. F. Silva, G. A. Atta Diab, N. L. Salas, A. Savateev, M. Antonietti, *J. Mater. Chem. A* **2022**, *10*, 18156.
- [12] a) J. Jiang, L. Ou-Yang, L. Zhu, A. Zheng, J. Zou, X. Yi, H. Tang, *Carbon* **2014**, *80*, 213; b) P. Jiménez-Calvo, C. Marchal, T. Cottineau, V. Caps, V. Keller, *J. Mater. Chem. A* **2019**, *7*, 14849.
- [13] V. W.-H. Lau, I. Moudrakovski, T. Botari, S. Weinberger, M. B. Mesch, V. Duppel, J. Senker, V. Blum, B. V. Lotsch, *Nat. Commun.* **2016**, *7*, 12165.
- [14] J. Yuan, X. Liu, Y. Tang, Y. Zeng, L. Wang, S. Zhang, T. Cai, Y. Liu, S. Luo, Y. Pei, C. Liu, *Appl. Catal. B* **2018**, *237*, 24.
- [15] J. F. Sonnenberg, N. Coombs, P. A. Dube, R. H. Morris, *J. Am. Chem. Soc.* **2012**, *134*, 5893.
- [16] a) D. Dvoranová, Z. Barbieriková, V. Brezová, *Molecules* **2014**, *19*, 17279; b) L. Khachatryan, E. Vejerano, S. Lomnicki, B. Dellinger, *Environ. Sci. Technol.* **2011**, *45*, 8559.
- [17] G. R. Buettner, *Free Radical Biol. Med.* **1987**, *3*, 259.
- [18] J. Wang, Y. Yu, J. Cui, X. Li, Y. Zhang, C. Wang, X. Yu, J. Ye, *Appl. Catal.* **2022**, *301*, 120814.
- [19] J. Ma, T. J. Miao, J. Tang, *Chem. Soc. Rev.* **2022**, *51*, 5777.
- [20] J. Hohenberger, K. Ray, K. Meyer, *Nat. Commun.* **2012**, *3*, 720.
- [21] D. Abdullin, N. Fleck, C. Klein, P. Brehm, S. Spicher, A. Lützen, S. Grimme, O. Schiemann, *Chem.-Eur. J.* **2019**, *25*, 2586.
- [22] Y. Kim, J. Kim, L. K. Nguyen, Y.-M. Lee, W. Nam, S. H. Kim, *Inorg. Chem. Front.* **2021**, *8*, 3775.
- [23] E. Andris, R. Navrátil, J. Jašík, T. Terencio, M. Srnc, M. Costas, J. Roithová, *J. Am. Chem. Soc.* **2017**, *139*, 2757.
- [24] a) S. Park, K. Jin, H. K. Lim, J. Kim, K. H. Cho, S. Choi, H. Seo, M. Y. Lee, Y. H. Lee, S. Yoon, M. Kim, H. Kim, S. H. Kim, K. T. Nam, *Nat. Commun.* **2020**, *11*, 5230; b) R. S. Czernuszewicz, Y. O. Su, M. K. Stern, K. A. Macor, D. Kim, J. T. Groves, T. G. Spiro, *J. Am. Chem. Soc.* **1988**, *110*, 4158.
- [25] a) S. P. Cramer, F. M. F. Degroot, Y. Ma, C. T. Chen, F. Sette, C. A. Kipke, D. M. Eichhorn, M. K. Chan, W. H. Armstrong, E. Libby, G. Christou, S. Brooker, V. Mckee, O. C. Mullins, J. C. Fuggle, *J. Am. Chem. Soc.* **1991**, *113*, 7937; b) M. G. Delcey, R. Lindblad, M. Timm, C. Bülow, V. Zamudio-Bayer, B. Von Issendorff, J. T. Lau, M. Lundberg, *Phys. Chem. Chem. Phys.* **2022**, *24*, 3598.
- [26] A. Braun, L. B. Gee, M. W. Mara, E. A. Hill, T. Kroll, D. Nordlund, D. Sokaras, P. Glatzel, B. Hedman, K. O. Hodgson, A. S. Borovik, M. L. Baker, E. I. Solomon, *J. Am. Chem. Soc.* **2023**, *145*, 18977.
- [27] a) W. Nam, Y.-M. Lee, S. Fukuzumi, *Acc. Chem. Res.* **2014**, *47*, 1146; b) X. Huang, J. T. Groves, *J. Biol. Inorg. Chem.* **2017**, *22*, 185.
- [28] J. Jung, S. Kim, Y.-M. Lee, W. Nam, S. Fukuzumi, *Angew. Chem., Int. Ed.* **2016**, *55*, 7450.
- [29] a) N. Y. Oh, Y. Suh, M. J. Park, M. S. Seo, J. Kim, W. Nam, *Angew. Chem., Int. Ed.* **2005**, *44*, 4235; b) L. Deng, T. Ziegler, *Organometallics* **1997**, *16*, 716.
- [30] a) R. Y. Liu, M. M. Trinh, M. B. Chang, *Sustain. Environ. Res.* **2022**, *32*, 10; b) Y.-E. Lee, W.-C. Chung, M.-B. Chang, *Environ. Sci.* **2019**, *26*, 20908; c) H. Einaga, K. Mochiduki, Y. Teraoka, *Catalysts* **2013**, *3*, 219; d) H. Einaga, *Appl. Catal. B* **2002**, *38*, 215.
- [31] a) Y.-X. Tan, Z.-M. Chai, B.-H. Wang, S. Tian, X.-X. Deng, Z.-J. Bai, L. Chen, S. Shen, J.-K. Guo, M.-Q. Cai, C.-T. Au, S.-F. Yin, *ACS Catal.* **2021**, *11*, 2492; b) K. Su, H. Liu, B. Zeng, Z. Zhang, N. Luo, Z. Huang, Z. Gao, F. Wang, *ACS Catal.* **2020**, *10*, 1324; c) X. Cao, Z. Chen, R. Lin, W.-C. Cheong, S. Liu, J. Zhang, Q. Peng, C. Chen, T. Han, X. Tong, Y. Wang, R. Shen, W. Zhu, D. Wang, Y. Li, *Nat. Catal.* **2018**, *1*, 704.
- [32] a) T. H. Yosca, J. Rittle, C. M. Krest, E. L. Onderko, A. Silakov, J. C. Calixto, R. K. Behan, M. T. Green, *Science* **2013**, *342*, 825; b) C. Limberg, *Angew. Chem., Int. Ed.* **2003**, *42*, 5932.
- [33] S. Stoll, A. Schweiger, *J. Magn. Reson.* **2006**, *178*, 42.
- [34] L. Braglia, M. Fracchia, P. Ghigna, A. Minguzzi, D. Meroni, R. Edla, M. Vandichel, E. Ahlberg, G. Cerrato, P. Torelli, *J. Phys. Chem. C* **2020**, *124*, 14202.
- [35] T. J. Regan, H. Ohldag, C. Stamm, F. Nolting, J. Lüning, J. Stöhr, R. L. White, *Phys. Rev. B* **2001**, *64*, 214422.
- [36] B. Gilbert, C. H. Frazer, A. Belz, P. G. Conrad, K. H. Nealson, D. Haskel, J. C. Lang, G. Srajer, G. De Stasio, *J. Phys. Chem. A* **2003**, *107*, 2839.
- [37] E. Stavitski, F. M. F. De Groot, *Micron* **2010**, *41*, 687.
- [38] G. van der Laan, in *Magnetism: A Synchrotron Radiation Approach. Lecture Notes in Physics* (Eds.: E. Beaurepaire, H. Bulou, F. Scheurer, J. P. Kappler), Springer, Berlin/Heidelberg, Germany **2006**.